

The Ly α forest at redshifts 0.1 – 1.6: good agreement between a large hydrodynamic simulation and HST spectra

Pascal Paschos*, Tridivesh Jena, David Tytler, David Kirkman

and Michael L. Norman

Center for Astrophysics and Space Sciences, University of California San Diego, La Jolla, CA, 92093-0424

5 November 2018

ABSTRACT

We give a comprehensive statistical description of the Ly α absorption from the intergalactic medium in a hydrodynamic simulation at redshifts 0.1 – 1.6, the range of redshifts covered by spectra of QSOs obtained with the Hubble Space Telescope. We use the ENZO code to make a simulation in a cube with side length 76 Mpc comoving using 75 kpc cells, for a Hubble constant of 71 km s $^{-1}$ Mpc $^{-1}$. The best prior work, by Davé et al. (1999), used an SPH simulation in a 15.6 Mpc box with an effective resolution of 245 kpc and slightly different cosmological parameters. We use a popular cosmological model and astrophysical parameters that describe the ultraviolet background that photoionizes and heats the gas. At redshifts $z = 2$ this simulation is different from data. Tytler et al. (2007) found that the simulated spectra at $z = 2$ have too little power on large scales, Ly α lines are too wide, there is a lack high column density lines, and there is a lack of pixels with low flux. Here we present statistics at $z < 1.6$, including the flux distribution, the mean flux, the effective opacity, and the power and correlation of the flux. We also give statistics of the Ly α lines including the line width distribution, the column density distribution, the number of lines per unit equivalent width and redshift, and the correlation between the line width and column density. We find that the mean amount of absorption in the simulated spectra changes smoothly with redshift with $DA(z) = 0.0102(1+z)^{2.252}$. Both the trend and absolute values are close to measurements of HST spectra by Kirkman et al. (2007). The column density distribution and the line width distribution are also close to those measured from HST spectra by Janknecht et al. (2006), except for the mode of the line width distribution which is smaller in the HST spectra, probably because of photon noise. Although some differences that we saw at $z = 2$ are too subtle to be seen in existing HST spectra, overall, the simulation gives a good description of HST spectra at $0.1 < z < 1.6$.

Key words: quasars: absorption lines – cosmology: observations – intergalactic medium – numerical simulations.

1 INTRODUCTION

We are exploring the physical conditions in the IGM using hydrodynamic numerical simulations. Our goal is to make simulations that give simulated H I Ly α absorption that is statistically identical to that measured in spectra of QSOs, where the best data give errors on the statistics of a few percent. We hope that such simulations will provide a com-

prehensive, accurate and reliable description of the physical conditions in the IGM.

In previous papers we compared our optically thin ENZO simulations to data at redshifts $z \sim 2$. In Jena et al. (2005)(J05) we found that popular values of cosmological and astrophysical parameters gave simulated spectra that simultaneously match both the the mean amount of Ly α absorption and the distribution of Ly α line widths in ground based spectra of QSOs. In Tytler et al. (2007) however, we found that the same simulation does not simultaneously

* E-mail: ppaschos@minbari.ucsd.edu

match other statistics measured in data. The power spectrum of the flux in the simulated spectra has significantly lower amplitude than we measure in data, by 50% on large scales and 20% on small scales. The lines in the simulated spectra are wider with larger b -values, and the simulated spectra have different distributions for both the flux per pixel and the number of lines at various column densities than do the data. Here we use the same simulation to explore redshifts 0.1 – 1.6 where the Ly α line is visible in spectra obtained from space.

Davé et al. (1999) used SPH simulations to explore the Ly α forest at these low redshifts. One of their simulations used cosmological parameters close to those favoured today: $\Omega_m = 0.4$, $\Omega_b = 0.0473$, $\Omega_\Lambda = 0.6$, $h = 0.65$ and $\sigma_8 = 0.8$. However, they used a box only 15.6 Mpc (we use a Hubble constant of $71 \text{ km s}^{-1} \text{ Mpc}^{-1}$ throughout the paper) on a side and an effective resolution of 245 kpc, both far from ideal. It is now well known (Pen 1997; Barkana & Loeb 2004; Sirko 2007; Tytler et al. 2007), that we need box sizes of the order of a hundred Mpc to contain the long mode density perturbations. In smaller boxes, we lack these long wavelength modes and we see significantly lower velocities and temperatures at all densities including those that make the Ly α forest (Tytler et al. 2007). We also require small enough cells that we can effectively resolve the structures in the Ly α forest. Meiksin & White (2004) found that the ideal cell size is < 40 kpc and in Tytler et al. (2007) we confirm this. The 75 kpc cells that we use here are large enough that the line widths are significantly larger than they would be with much smaller cells. J05 showed that a cell size of 150 kpc gives a poor representation of the IGM, sometimes showing trends with input parameters that are the opposite of what we see with small cells that resolve the Ly α forest.

In §2 below, we briefly describe the simulation code and parameters we have adopted. In §3 we describe the statistics of the flux in the Ly α forest including the mean flux, flux distribution and the flux power and autocorrelation function. In §4 we describe the statistics of the lines in the Ly α forest including the b -values, column densities and their correlations. In §5 we give a brief comparison to data from HST. We discuss and conclude in §6.

2 ENZO IGM SIMULATIONS

The numerical simulation that we describe in this paper (Bodenheimer et al. 2007) uses the Eulerian hydrodynamic cosmological code ENZO (Bryan et al. 1995; Bryan & Norman 1997; Norman & Bryan 1999; O’Shea et al. 2004; O’Shea et al. 2005; Regan et al. 2007; Norman et al. 2007). The simulation contains both CDM and baryons in the form of gas, but no stars. The simulation was run with popular values for cosmological parameters: a flat geometry $\Omega_{total} = 1$, comprising a vacuum energy density of $\Omega_\Lambda = 0.73$, $\Omega_m = 0.27$ (CDM plus baryons), a baryon density of $\Omega_b = 0.044$, a Hubble constant of $H_0 = 71 \text{ km s}^{-1} \text{ Mpc}^{-1}$ and an initial power spectrum scalar slope of $n_s = 1.0$ with a current amplitude of $\sigma_8 = 0.9$.

The ENZO code follows the evolution of the gas using non-equilibrium chemistry and cooling for hydrogen and helium ions (Abel et al. 1997; Anninos et al. 1997). After reionization at $z = 6$, photoionization is provided using the

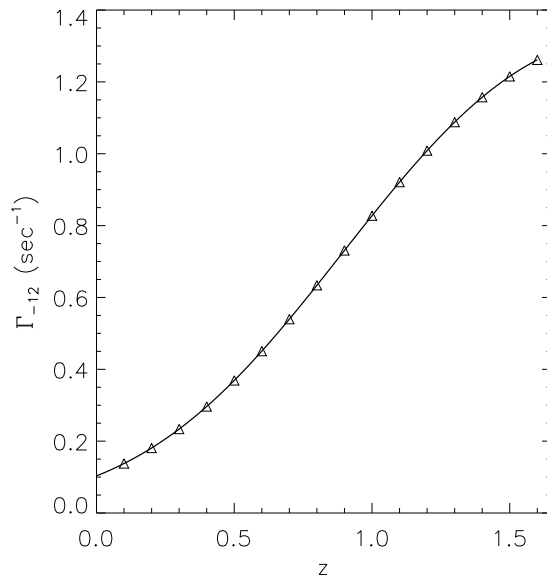


Figure 1. The photoionization rate from the UV emitted by QSOs and galaxies calculated by Haardt & Madau (2001) that we use in this simulation. The vertical axis is in units of 10^{-12} photoionization per neutral H atom per second.

Haardt & Madau (2001) volume average UV background (UVB) from an evolving population of galaxies and QSOs. We show the rate of ionization of neutral hydrogen in Fig. 1

The simulations are optically thin so that all cells experience the same UV intensity at a given time. We do not treat the transfer of radiation inside the volume, and we include no feedback from individual stars, galaxies or QSOs except for that implied by the uniform UVB.

As in J05, we use two astrophysical parameters to describe the intensity of the UVB. The parameter γ_{912} is the rate of ionization per H I atom in units of the Haardt & Madau model discussed above, while X_{228} measures the heat input per He II ionization, again in units of the rate for the Haardt & Madau spectrum. In J05 we showed how we can use X_{228} to adjust the widths of the Ly α lines and the mean amount of absorption in simulated spectra, while γ_{912} will also adjust the mean amount of absorption. We can then choose values for X_{228} and γ_{912} that together match both the line widths and mean flux in data. The simulation that we discussed in this paper uses $\gamma_{912} = 1.0$ and $X_{228} = 1.8$, and we called it simulation or box A in Jena et al. (2005)(J05) and Tytler et al. (2007).

We initiate the simulations using an Eisenstein & Hu (1999) power spectrum for the dark matter perturbations, that we insert at $z = 60$. The simulated volumes are all cubes with strictly periodic boundary conditions. Hence the power is input at a finite number of discrete wavenumbers.

The amplitude of the power that we insert varies smoothly with wavenumber. We insert the amplitude expected for the universe as a whole, with no random variations associated with the finite box sizes. The power in the simulations is not adjusted to include the variations in mean density that we see in the universe on the scale of the boxes.

In this limited sense, the boxes contain information on scales much larger than their sizes.

The simulation has a comoving box size of 76.8 Mpc and a comoving cell size of $53.25h^{-1}$ or 75 kpc comoving. The simulation has one CDM particle for each cell initially, and each dark matter particle has a mass of $M_{CDM} \simeq 9.5 \times 10^6 h^{-1} M_{\odot}$.

Our simulation is barely large enough that the values we obtain at $z = 0.1$ will be reliable. The nonlinear scale can be quantified by calculating the wavenumber k_{NL} such that $\frac{1}{(2\pi)^3} \int_0^{k_{NL}} P^{3D}(k) 4\pi k^2 dk = 1$ where $P^{3D}(k)$ is the three dimensional matter power spectrum. This indicates that the nonlinear scale is 14.11 Mpc (comoving) at $z = 1.6$ and 25.51 Mpc (comoving) at $z = 0.1$. These correspond to 18.38% of the box size at $z = 1.6$ and 33.22% of the box size at $z = 0.1$. In smaller boxes, the largest modes that fit inside the box have become non-linear before this low redshift and the results will be unreliable.

2.1 Comparison of this simulation to data at $z = 2$

In Jena et al. (2005)(J05) we showed that at redshift 1.95 various simulations using typical cosmological and astrophysical parameters gave a good match to both the mean flux transmitted in the Ly α forest and the b -value distribution that we use to describe the line widths. We noted in Fig. 40 of J05 that the power spectrum of the flux for these simulations was similar to that of data, but we did not examine this in detail.

In Tytler et al. (2007) we compared a wider variety of statistics at $z = 2$ to the simulations that we use in this paper, and to other simulations using the same input parameters in smaller boxes. We found that if we matched the mean flux well, the line widths in the simulation were too big using $\sigma_8 = 0.9$ and $X_{228} = 1.8$ times the standard UVB heating. If we instead use the smaller σ_8 values preferred by the WMAP 3 year data, the lines in the simulated spectra would be still larger. We now know that we could better match the line widths using $X_{228} < 1.8$, corresponding to a softer ionizing spectrum that gives less heating. However, from Fig. 39 of J05, we would simultaneously need to use $\gamma_{912} > 1$ to preserve the match with the mean absorption, and hence it is unclear whether the combination of X_{228} and γ_{912} parameters would be concordant with other data.

We also found that the simulated spectra had too little power on both small and large scales. The small scales are an alternative way of noticing that the lines are too wide in the simulations. However, the larger scales are harder to adjust. We might use a larger σ_8 value or we might need to adjust the heating.

We found that our simulations have too many lines with $\log N_{HI} < 14 \text{ cm}^{-2}$, a slight lack of lines with $\log N_{HI} = 14\text{--}15 \text{ cm}^{-2}$ and a large lack with $\log N_{HI} > 17 \text{ cm}^{-2}$. We did not investigate whether these differences are themselves enough to account for the missing power. We also found, confirming Bolton et al. (2007), that our simulated spectra have too few pixels with a lot of absorption.

We concluded that there were three classes of changes that might allow us to make simulations that exactly match data.

First, there might be problems with the simulations. We

use moderate resolution optically thin simulations that we hope will match the low density IGM. Tytler et al. (2007) showed that using a much larger box does not help, while a factor of four smaller cell size made the difference larger. Kohler & Gnedin (2007) showed that they obtain the correct number of Lyman limit systems (LLS, with $\log N_{HI} > 17.2 \text{ cm}^{-2}$) at $z = 4$ using 2 kpc cells with radiative transfer. Perhaps a much larger version of their simulation might also match the entire column density distribution, the power, line widths and flux distribution. We should certainly add radiative transfer, especially that associated with the ionization of He II by discrete sources. This should give more realistic temperatures and may improve the match to the data (Bolton et al. 2007). Early results such as Bolton et al. (2004) and Paschos et al. (2007) show that radiative transfer increases the temperature of the IGM at the cosmic mean density, the opposite of what we need. However radiative transfer might also give lower temperatures at the higher densities that make the Ly α forest (Bolton et al. 2007).

A second option is to change the astrophysics and especially the heating of the IGM. A softer UVB will probably make spectra that are more like data. The third choice is to change the cosmological parameters, specifically we expect that a simulation with $\sigma_8 > 0.9$ would make spectra with more large scale power, more like the data.

In summary, we know that our simulation is not ideal, but they are as good as any yet done, and a major improvement on those published at $z < 2$.

When we compare simulations to data we would like to concentrate on the low density IGM that we can most readily simulate. We take this to mean $\log N_{HI} < 17 \text{ cm}^{-2}$ since the lack of lines becomes much larger at higher column densities and it is relatively easy to find Lyman continuum absorption in real spectra. At $z = 2$ the simulations contain some such lines, but factors of many less than there are in real spectra (Tytler et al. 2007, Fig. 15). Many of the statistics that we show below include lines of all column densities, including the few lines with $\log N_{HI} > 17 \text{ cm}^{-2}$ in our simulated spectra. We will be analysing 2000 spectra at each redshift from 0.1 to 1.6. These spectra contain no lines with $\log N_{HI} > 17 \text{ cm}^{-2}$ at $z = 0.1$ and 26 such lines at $z = 1.6$.

3 STATISTICS OF THE FLUX IN THE Ly α FOREST

We make spectra of the flux transmitted through the IGM at Ly α wavelengths using the code described in J05 and following the improvements discussed in Tytler et al. (2007). We made 2000 spectra, each parallel to z -axis of the box and beginning at a random location on the xy -face of the box. We made 2000 spectra at each redshift from 0.1 – 1.6, in steps of 0.1. The random numbers that selects the x, y coordinates of each spectrum on the cube's face were different at each redshift and hence these spectra are approximately independent, except that they all sample the same large scales structure in the box.

We use a number of pixels per spectrum equal to the number of cells along a box side. We calculate the optical depth as a function of velocity in a spectrum, $\tau(v)$, using equations in §4 of J05, and the flux from $F = \exp(-\tau)$,

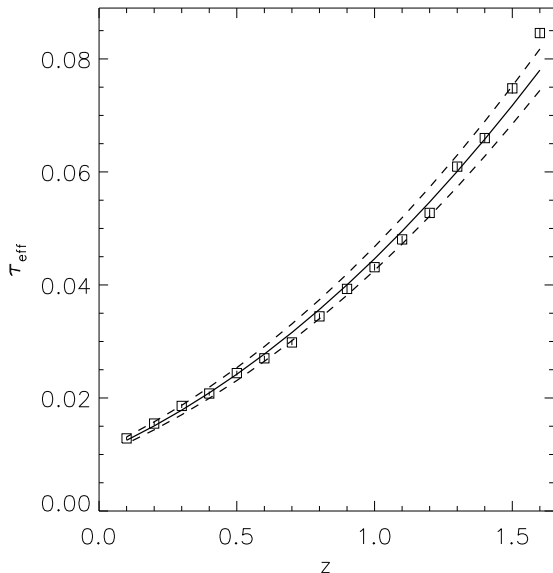


Figure 3. The effective opacity and a power law fit. The fit is a function of the form $\tau_{eff}^{fit} = A(1+z)^\alpha$ where z is the redshift, $A = 0.0102$ and $\alpha = 2.252$. The curves above and below the solid line are best fits to the 2σ upper and lower limits on the individual points. They do not show the range of possible fits.

where $F = 1.0$ in the absence of absorption, and $F \rightarrow 0$ at the centre of saturated absorption lines. The spectra from all simulations are smooth functions of v , with no discreteness from the cell size, because to determine τ at each position we integrate over at least ± 512 cells, to the left and to the right of the absorbing cell. Each spectrum is made at a fixed redshift. We convert from the Mpc per grid cell into velocity v in km s^{-1} of a spectrum using the $H(z)$ for the chosen z , but we do not increment the z as we move down a sight line, and we do not change the $H(z)$. Each spectrum is then frozen at the indicated redshift with no evolution.

In Fig. 2 we show examples of the spectra. At lower redshifts we see systematically less absorption in total, fewer strong lines with large equivalents, and more regions with less than 5% absorption.

3.1 Effective Opacity

In Fig. 3 we show the mean effective opacity as a function of redshift. We calculate the effective opacity from the mean flux \bar{F} using $\tau_{eff} = -\ln(\bar{F})$, as is normally done. The mean flux is the mean of all spectra that we made at each redshift. In Table 1 we give values for this and other statistics that have a single value at each redshift.

We see that the effective opacity fall smoothly with decreasing redshift, from 0.085 at $z = 1.6$ to 0.013 at $z = 0.1$. This is well fit by the power law that we show.

3.2 Mean Amount of Absorption

We define DA , the mean amount of absorption, as $DA = 1 - \bar{F}$, where \bar{F} is the mean flux in all the spectra that we made at that z . In Fig. 4 we show the DA as a function

Table 1. Statistics of the Ly α forest at redshifts 0.1 to 1.6. Γ_{12} is the ionization rate in units of 10^{-12} ionizations per H atom per second. τ_{eff} is the mean effective optical depth, and DA the mean absorption. The values in the err column are 10^4 times the standard deviation of the DA values. Under σ_L^2 we give 10^3 times the variance in the mean flux in each spectrum. For σ^2 we list 100 times the variance in the mean flux in each pixel in all the spectra F_{mode} is the mode of the mean flux in each spectrum.

z	Γ_{-12}	τ_{eff}	DA	err (10^4)	σ_L^2 (10^3)	σ^2 (10^2)	F_{mode}
1.6	1.261	0.085	0.081	8.7	1.5	3.5	0.925
1.5	1.215	0.075	0.072	9.4	1.8	3.0	0.945
1.4	1.157	0.066	0.064	7.5	1.1	2.6	0.955
1.3	1.088	0.061	0.059	7.1	1.0	2.5	0.955
1.2	1.009	0.053	0.051	6.7	0.9	2.1	0.965
1.1	0.921	0.048	0.047	6.3	0.8	1.9	0.975
1.0	0.828	0.043	0.042	5.9	0.7	1.6	0.975
0.9	0.731	0.039	0.039	8.1	1.3	1.6	0.975
0.8	0.634	0.034	0.034	5.4	0.6	1.4	0.975
0.7	0.540	0.029	0.029	4.7	0.4	1.1	0.985
0.6	0.451	0.027	0.027	4.6	0.4	1.1	0.985
0.5	0.369	0.024	0.024	4.3	0.4	0.9	0.985
0.4	0.296	0.021	0.021	3.7	0.3	0.8	0.985
0.3	0.234	0.019	0.018	3.6	0.3	0.7	0.995
0.2	0.181	0.016	0.015	3.2	0.2	0.6	0.995
0.1	0.138	0.013	0.013	2.6	0.1	0.5	0.995

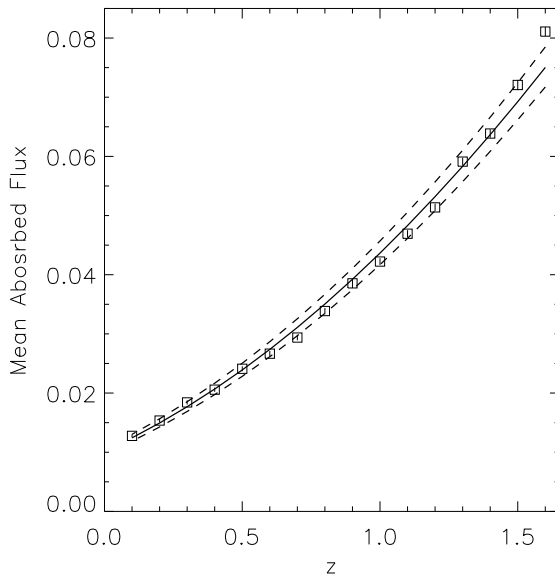


Figure 4. The mean absorption as a function of redshift. The solid line shows the fit through the points obtained from the optical depth fit $F_{fit} = \exp(-\tau_{eff}^{fit})$ in Fig. 3. The upper and lower curves are fits to the 2σ upper and lower limits on each point.

of redshift. Since the effective optical depth is $\tau_{eff} \ll 1$, we expect $DA = 1 - \bar{F} = 1 - \exp(-\tau_{eff}) \simeq \tau_{eff}$ as can be seen in the figure. The amount of absorption decreases by a factor of 6.2 from $z = 1.6$ to 0.1. We know from Jena et al. (2005) that had we used a simulation with a cell size of 18 kpc instead of the 75 kpc used here, the mean flux would be reduced by about 0.02 at $z = 2$.

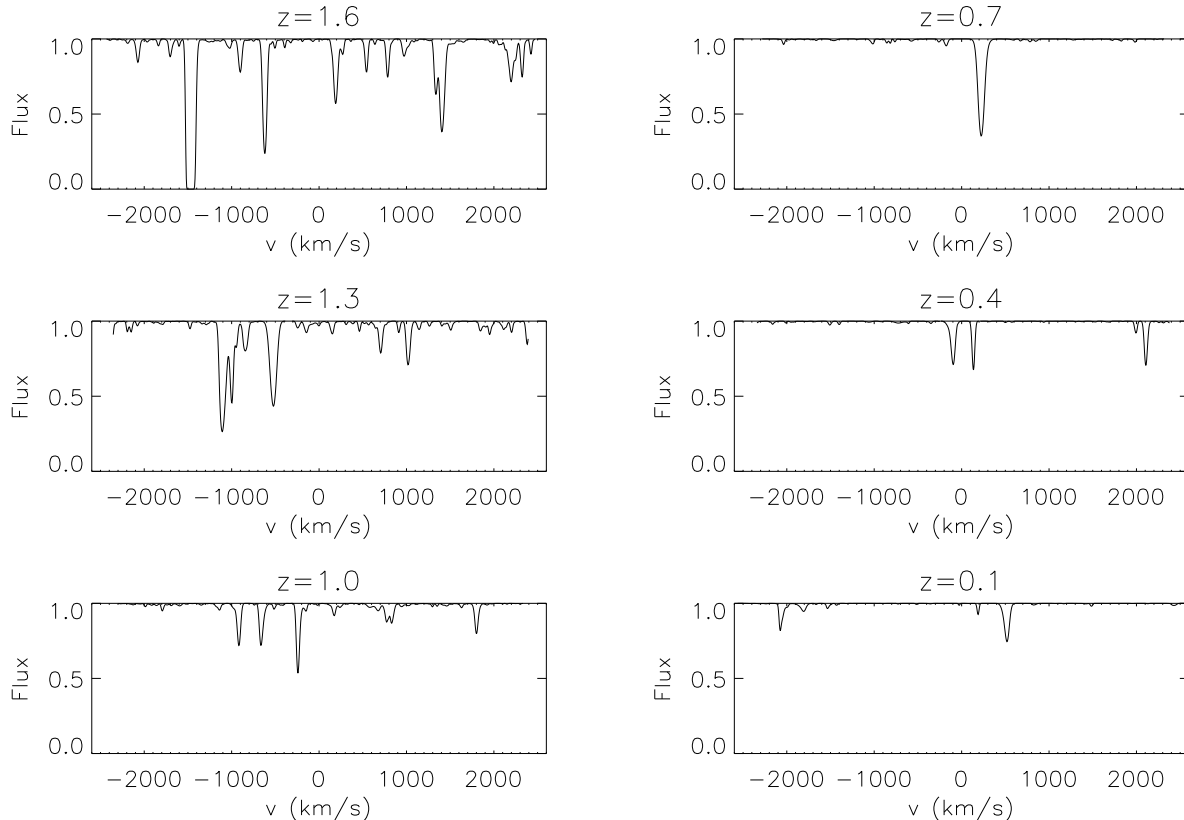


Figure 2. Spectra of the Ly α absorption from the simulation. For each redshift we choose to show a spectrum with a mean flux that is approximately the same as the mean flux of all the spectra at that z . Although the velocity span of the box, and hence the spectra, decreases with the Hubble constant at low redshifts, we plot the same velocity range for all spectra.

3.3 Distribution of Flux

In Fig. 5 we show the distribution of flux per pixel for all spectra through the box, the flux pdf. The flux pdf is the number of pixels in each range of flux, flux bins, divided by the total number of pixels and then divided by the bin width, which is 0.05. We have 1024 pixels per spectrum and 2000 spectra per redshift. Using this common definition, the values unfortunately depend on the bin width. Our bins are all the same width starting with the first bin at flux $0 < F < 0.05$ with a centre at 0.025, and a last bin at $0.95 < F < 1.0$. Our bin centres and the widths of two of our bins differ from Kim et al. (2007) and Bolton et al. (2007) who choose a first bin at flux $-0.025 < F < 0.025$ with a centre at 0, and a last bin at $0.975 < F < 1.025$ with a centre at 1.0. Since they divided all their bins by the same constant 0.05 (Kim private communication), their flux pdf changes slope abruptly in the first and last bins, being a factor of 2.0 below the value that we infer for flux zero and 1.0. We do not follow their definition because it is unexpected and hides trends.

In Fig. 5 we see a smooth and continuous change in the shape of the flux PDF with redshift. As the redshift falls, the fraction of pixels with $0.95 < F < 1.0$ increases while the fractions decline for all other flux value. At $z = 1.6$, 71% of pixels have $F > 0.95$ and only 1.2% have $F < 0.05$. At $z = 0.1$, 95.6% have $F > 0.95$ and 0.18% have $F < 0.05$. These values suggests that strong saturated lines that have

$F < 0.05$ are 6.7 times less common at $z = 0.1$ compared to $z = 1.6$. This rate of change is similar to the factor of 6.5 decrease in the effective optical depth and 6.2 in the mean amount of absorption.

The fractional changes in the flux pdf values are similar for all redshifts and fluxes, except for $F > 0.95$ where the curves for the different redshifts cross. In detail, we see a faster relative change with redshift at the lower fluxes; the curves spread out more to the left of the plot. This suggests that strong deep lines that correspond to higher column densities may evolve faster than do the weaker lines with smaller column densities, a trend that we will see more clearly in other statistics.

3.4 Flux power

We define the flux contrast as

$$f(u) = (F/\bar{F}) - 1, \quad (1)$$

where u is velocity and \bar{F} is the mean flux from the all spectra that we made at a given z . We measure the one-dimensional flux power of each sight line in the z direction by computing the fourier transform of the flux contrast, and we present the average of the power from all sight lines at a given z in Fig. 6. The smallest k value that we show is that for one wave along an edge of the box. This is a constant in

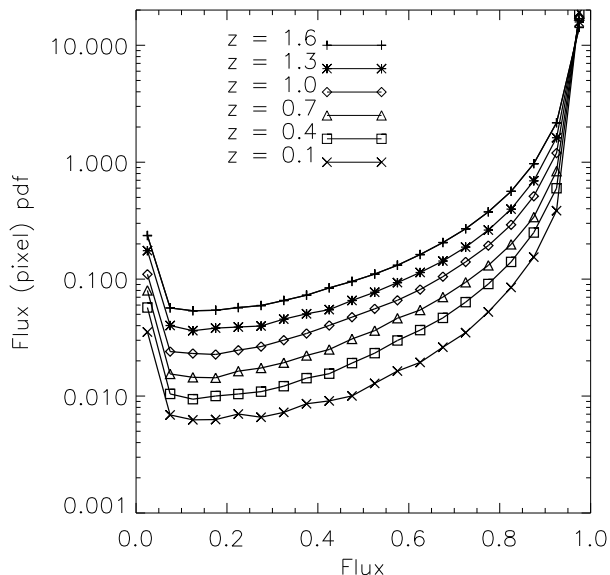


Figure 5. The pdf of the flux per pixel. We use flux bins of width 0.05 from 0.0 – 1.0, and we plot values at the bin centres, 0.025, 0.075, ..., 0.975.

Table 2. The flux pdf at different redshifts. The first column is the redshift of the bin centre while the rest of the columns are the flux PDF values at different redshifts. All bins have a width of 0.05, starting with the first bin from flux 0 – 0.05. The pdf values in the bulk of the table are the fraction of pixels with flux value in the bin, divided by 0.05. The flux pdf values in each column sum to 1/0.05.

flux	redshift					
	1.6	1.3	1.0	0.7	0.4	0.1
0.025	0.236	0.175	0.110	0.080	0.057	0.0354
0.075	0.057	0.040	0.024	0.015	0.011	0.0069
0.125	0.054	0.036	0.023	0.014	0.009	0.0062
0.175	0.054	0.038	0.023	0.014	0.010	0.0063
0.225	0.057	0.039	0.025	0.016	0.010	0.0070
0.275	0.059	0.040	0.026	0.017	0.011	0.0066
0.325	0.066	0.045	0.030	0.019	0.012	0.0072
0.375	0.073	0.050	0.034	0.022	0.014	0.0086
0.425	0.084	0.055	0.040	0.025	0.015	0.0091
0.475	0.095	0.066	0.047	0.031	0.019	0.0100
0.525	0.110	0.077	0.056	0.036	0.023	0.0128
0.575	0.131	0.093	0.066	0.046	0.030	0.0164
0.625	0.162	0.114	0.081	0.054	0.037	0.0194
0.675	0.207	0.143	0.105	0.070	0.047	0.0261
0.725	0.269	0.188	0.140	0.094	0.063	0.0348
0.775	0.376	0.263	0.193	0.131	0.091	0.0523
0.825	0.563	0.396	0.291	0.198	0.140	0.0849
0.875	0.972	0.693	0.511	0.339	0.250	0.1543
0.925	2.174	1.620	1.197	0.838	0.598	0.3848
0.975	14.201	15.828	16.970	17.937	18.551	19.1107

comoving Mpc, but in velocity units it falls with the decrease in the Hubble constant at low redshifts.

We could compute the autocorrelation of the flux for a given velocity lag δu directly from a flux spectrum as $\xi_F(\delta u) = \langle (F(u) - \bar{F})(F(u + \delta u) - \bar{F}) \rangle$, where \bar{F} is the mean flux for all spectra at that z and the brackets refer

Table 3. The flux power at different redshifts at selected values of the wavenumber k (s/km). The first column lists the redshifts while the next four columns list the value of the logarithm of the flux power at the wavenumber listed on top of each column.

z	$\log k$			
	-2.0	-1.5	-1.0	-0.5
1.600	0.502	0.050	-1.382	-4.711
1.500	0.417	0.005	-1.395	-4.693
1.400	0.375	-0.042	-1.398	-4.656
1.300	0.331	-0.064	-1.386	-4.541
1.200	0.251	-0.132	-1.397	-4.462
1.100	0.208	-0.167	-1.393	-4.342
1.000	0.119	-0.223	-1.375	-4.261
0.900	0.069	-0.256	-1.360	-4.118
0.800	-0.018	-0.310	-1.361	-4.043
0.700	-0.088	-0.376	-1.363	-3.919
0.600	-0.148	-0.396	-1.347	-3.791
0.500	-0.206	-0.439	-1.348	-3.645
0.400	-0.338	-0.532	-1.356	-3.537
0.300	-0.367	-0.578	-1.362	-3.425
0.200	-0.496	-0.692	-1.410	-3.346
0.100	-0.641	-0.776	-1.413	-3.232

to an average across the pixels of the spectrum. Instead we choose to obtain the autocorrelation from

$$\xi_F(\delta u) = \frac{\bar{F}^2}{2\pi} \int P(k) e^{jk\delta u} dk \quad (2)$$

where $P(k)$ is the power of the flux contrast and we can use the line of sight averaged power directly because we have divided by the mean flux of the spectra at that z . In Fig. 7 we show the average autocorrelation profiles at each velocity lag from all lines of sight.

In Figs. 6 and 7 we again see clear systematic trends with z . As the redshift decreases the power drops on large scales $\log k < -1.0$ s/km, and increases on small scales. The power changes by less than a few percent at $\log k = -1.0$ s/km (a wavelength of 62 km s⁻¹) for $0.1 < z < 1.6$. The decrease in power on larger scales at lower redshifts comes from the decrease in the mean amount of absorption as the ionization of the IGM increases. The increase in the power on small scale (large k) at low z implies that the Ly α lines are narrower at low z , which we will see is correct in §4.2. As we saw in J05, had we used a cell size of about 18 kpc, the flux power at $z = 2$ would fall by about 15% at $k = 0.03$ and about 22% at $k = 0.01$ s/km.

The autocorrelation falls smoothly with both redshift and distance. It does not show the crossing of curves that we saw for the power.

3.5 Distribution of the mean flux per spectrum

In Fig. 8 we show the distribution of mean flux per line of sight. We calculate the mean flux in each spectrum, and we plot the fraction of the 2000 spectra with a given mean flux. This statistic depends on the length of the spectra, which is 76 Mpc comoving. We would see less variation in the mean flux in longer spectra. As the redshift decreases the distributions shift to the right, to larger mean fluxes, and the distributions become narrower, with less variation from spectrum to spectrum. None of the spectra at $z = 1.6$ has a mean flux > 0.98 , where as these are the most common mean

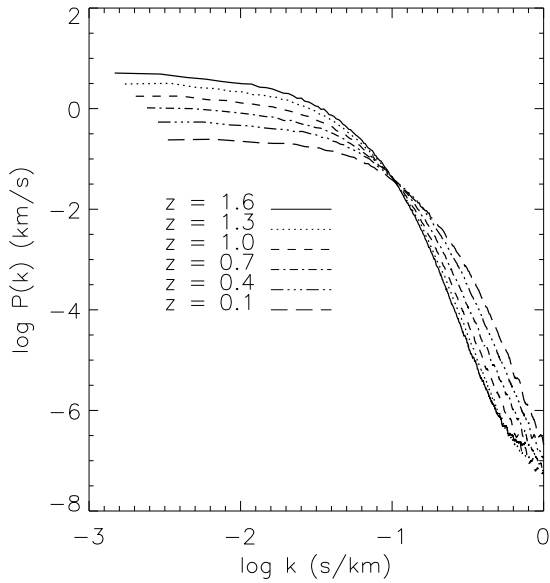


Figure 6. The mean 1D flux power from all 2000 spectra at each redshift. We list the values in Table 3.

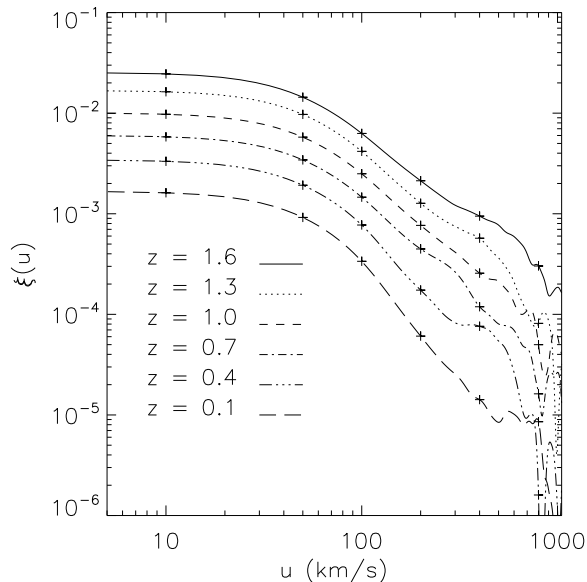


Figure 7. The flux autocorrelation function against the velocity lag. We use arbitrary curves to connect the points at a given redshift.

fluxes at $z = 0.1$. These distributions, especially the tail containing the occasional spectrum with a lot of absorption, reflect both the approximately exponential distribution of Ly α line equivalent widths and the clustering of matter on large scales.

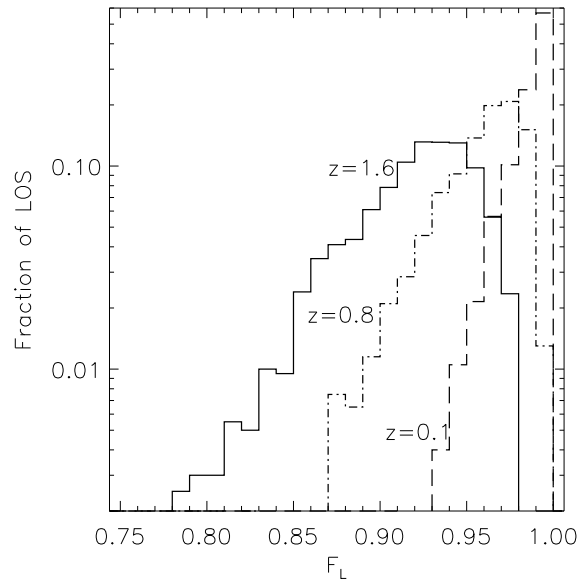


Figure 8. The fraction of spectra, one per line of sight (LOS), with a given mean flux F_L .

4 LYMAN α LINE STATISTICS

We obtain line statistics by fitting Voigt profiles as described in Zhang et al. (1997). As in Tytler et al. (2004) and J05 (§5.1, 6.2) for many functions and statistics we consider only lines with $12.5 < \log N_{\text{HI}} < 14.5 \text{ cm}^{-2}$.

We shall examine two sample of lines; a full sample of all lines with central optical depths $\tau_o > 10^{-5}$ and a sub-sample with $\tau_o > 0.05$. A sample that was largely complete to central optical depths $\tau_o > 0.05$ would require high enough resolution (FWHM $< 10 \text{ km s}^{-1}$) to completely resolve all the narrowest lines that would otherwise appear too shallow. The SNR per pixel must exceed 20 to give 1σ in the centres of the limiting lines, barely enough to detect a line that is several pixels wide. To detect most lines with $\tau_o = 0.05$ we would prefer SNR > 60 . The sample with $\tau_o > 10^{-5}$ includes a large number of additional shallow very low column density “lines” that are minor fluctuations in the flux. Existing HST spectra have far too low SNR to show such features.

4.1 Line widths as a function of column density

In Fig. 9 we show the b -values that quantify line width and H I column densities for Ly α lines in spectra at redshifts 1.6 and 0.1. We show only a fraction of all lines in our spectra at $z = 1.6$ to avoid saturating the plot. We show a curve on the plots that marks lines with line centre optical depth $\tau_o = 0.05$. From (Spitzer 1978),

$$N_{\text{HI}} = \sqrt{\pi} \tau_o b / \sigma_o \lambda_o, \quad (3)$$

where λ_o is the rest frame wavelength and σ_o is the cross-section. The curve has equation

$$b \text{ (km s}^{-1}\text{)} = 15.0(0.05/\tau_o)(N_{\text{HI}}/10^{12} \text{ cm}^{-2}), \quad (4)$$

and appears concave on the log-linear plots.

Table 4. The distribution of H I column density values in Ly α lines. We list values of $\log f(N_{\text{HI}})$ as a function of $\log N_{\text{HI}}$ value in the first column and redshift given in the top row. We include all lines with line centre optical depth $\tau_o > 10^{-5}$. We use column density bins of width 0.2 for $\log N_{\text{HI}} = 12.0\text{--}16.0 \text{ cm}^{-2}$, and 0.5 for $\log N_{\text{HI}} = 16.0\text{--}18.0 \text{ cm}^{-2}$. We list N/A when there are no lines in the column density bin in any of our 2000 spectra at that z .

log N_{HI} cm^{-2}	redshift					
	1.6	1.3	1.0	0.7	0.4	0.1
12.0	-9.51	-9.53	-9.56	-9.62	-9.67	-9.78
12.2	-9.74	-9.79	-9.85	-9.92	-9.99	-10.15
12.4	-10.01	-10.07	-10.15	-10.23	-10.28	-10.37
12.6	-10.29	-10.38	-10.47	-10.54	-10.61	-10.71
12.8	-10.61	-10.71	-10.80	-10.90	-10.94	-11.02
13.0	-10.92	-11.04	-11.11	-11.21	-11.26	-11.36
13.2	-11.26	-11.37	-11.46	-11.55	-11.62	-11.77
13.4	-11.61	-11.71	-11.81	-11.88	-11.95	-12.16
13.6	-11.95	-12.06	-12.12	-12.24	-12.35	-12.51
13.8	-12.32	-12.43	-12.52	-12.65	-12.80	-12.92
14.0	-12.69	-12.79	-12.92	-13.04	-13.17	-13.30
14.2	-13.08	-13.17	-13.36	-13.51	-13.63	-13.58
14.4	-13.44	-13.60	-13.70	-13.84	-13.95	-14.05
14.6	-13.81	-13.97	-14.14	-14.14	-14.33	-14.33
14.8	-14.23	-14.30	-14.42	-14.65	-14.79	-14.70
15.0	-14.61	-14.66	-14.83	-14.97	-14.88	-15.02
15.2	-14.96	-15.08	-15.21	-15.20	-15.26	-15.33
15.4	-15.39	-15.35	-15.56	-15.50	-15.51	-15.60
15.6	-15.55	-15.55	-15.94	-15.81	-15.87	-16.37
15.8	-16.10	-15.93	-16.26	-16.23	-16.16	-16.20
16.0	-16.37	-16.27	-16.18	-16.78	-16.83	-16.94
16.5	-17.19	-17.27	-17.26	-17.40	-17.38	-17.69
17.0	-17.74	-18.17	-17.97	-17.85	-17.88	N/A
17.5	-18.47	-18.54	-18.68	-19.30	-19.23	N/A
18.0	-19.54	-19.95	-19.88	-19.80	N/A	-19.66

We also show on the plots a straight line that represents the increase in the minimum b -value as a function of $\log N_{\text{HI}}$. A visual examination of the plot shows no major changes in the distribution in the b - N plane with redshift, but we will see below that there are definite differences in the both the b and N distributions.

4.2 Column Density Distribution

In Table 4 we list values for the H I column density distribution, $f(N)$, lines per unit z , per spectrum and per unit linear column density. With this standard definition (Tytler 1987) the integral of $f(N)$ over a range of linear (not log) column densities gives the number of lines in that column density range per unit redshift:

$$\frac{dn(z)}{dz} = \int f(N)dN. \quad (5)$$

In Fig. 10 we show the $f(N)$ distribution. A power law is a fair approximation to the distribution at all the N values, although the plot scale obscures significant deviations. We also show on the plot the sub-sample of the lines with $\tau_o > 0.05$. This sub-sample contains all lines at all except the lowest columns $\log N_{\text{HI}} < 12.5 \text{ cm}^{-2}$. On the plot of $f(N)$ for $z = 0.1$ we show the fit to the $f(N)$ at $z = 1.6$ in addition to a fit to the $f(N)$ at $z = 0.1$. We see that there are fewer lines per unit z at lower z at all N values, and especially

at high N values. The slope of the $f(N)$ becomes slightly steeper at lower redshifts. As redshift drops, the number of lines with large column densities falls faster than the number with small columns.

4.3 The doppler parameter distribution

In Fig. 11 we show distribution of lines widths for redshifts 1.2 and 1.6, together with the Hui-Rutledge (Hui & Rutledge 1999) function,

$$\frac{dn}{db} = B \frac{b_\sigma^4}{b^5} \exp\left(-\frac{b_\sigma^4}{b^4}\right) \quad (6)$$

where dn/db is the number of lines per km s^{-1} per unit z . The Hui-Rutledge function has only one parameter, b_σ , that describes the typical line width, where the peak of the distribution is $b_{\text{peak}} = 0.9457b_\sigma$. In Tytler et al. (2004, Fig. 18) we showed that this function gave an excellent fit to the distribution of b -values at $z = 1.95$. The function is also an excellent representation of the data at all low redshifts. In detail, the data have a wider distribution than the function, with more more lines at both small and large b -values.

We show in Fig. 12 the b_σ parameter as a function of redshift. As previously, we show two different samples of lines; all lines with $\tau_o > 10^{-5}$ and the sub-sample with $\tau_o > 0.05$. In both cases, the b_σ falls smoothly with redshift from $\sim 26.5 \text{ km s}^{-1}$ at $z = 1.6$ to $\sim 24.5 \text{ km s}^{-1}$ at $z = 0.1$. The two samples give identical b_σ values because there are very few lines with $\tau_o < 0.05$ and $\log N_{\text{HI}} > 12.5 \text{ cm}^{-2}$, the minimum that we consider when we evaluate $f(b)$. We know from Jena et al. (2005) that a simulation with a cell size of 18 km s^{-1} would give b -values smaller by approximately 1.0%.

In Fig. 13 we show the $f(b)$ for redshifts 0.1 and 1.6, each divided by the number of lines per unit redshift with column densities $\log N_{\text{HI}} = 12.5\text{--}14.5 \text{ cm}^{-2}$, as listed in listed in Table 5. The distributions have very similar shapes, although there are clearly more lines with smaller b -value at low redshift.

We list in Table 5 the b_σ and the median b -value b_{med} (50% of values are smaller) as a function of redshift. We prefer the b_σ with high SNR spectra because this statistic isolates the most common line width and it is insensitive to the precise shape of the b -value distribution at low and high values. However in low SNR spectra, such as those from HST, the b_{med} may be advantageous because it is even less sensitive to the detailed shape of the distribution. In low SNR data, we expect a false excess of lines with low b -values and a lack of lines with large b -values.

4.4 The equivalent width distribution

Fig. 14 shows the distribution of the rest frame equivalent widths W_o for all lines at two redshifts. We list values in Table 6.

Fig. 15 shows for two redshifts the number of lines with $W_o > W_o^t$, some minimum equivalent width. We find that a pair of straight lines can represent the points at each redshift, hence the distributions are approximately broken exponentials; $\ln(dn/dz) \propto W_o^t$.

In Fig. 16 we show how the number of lines with $W_o >$

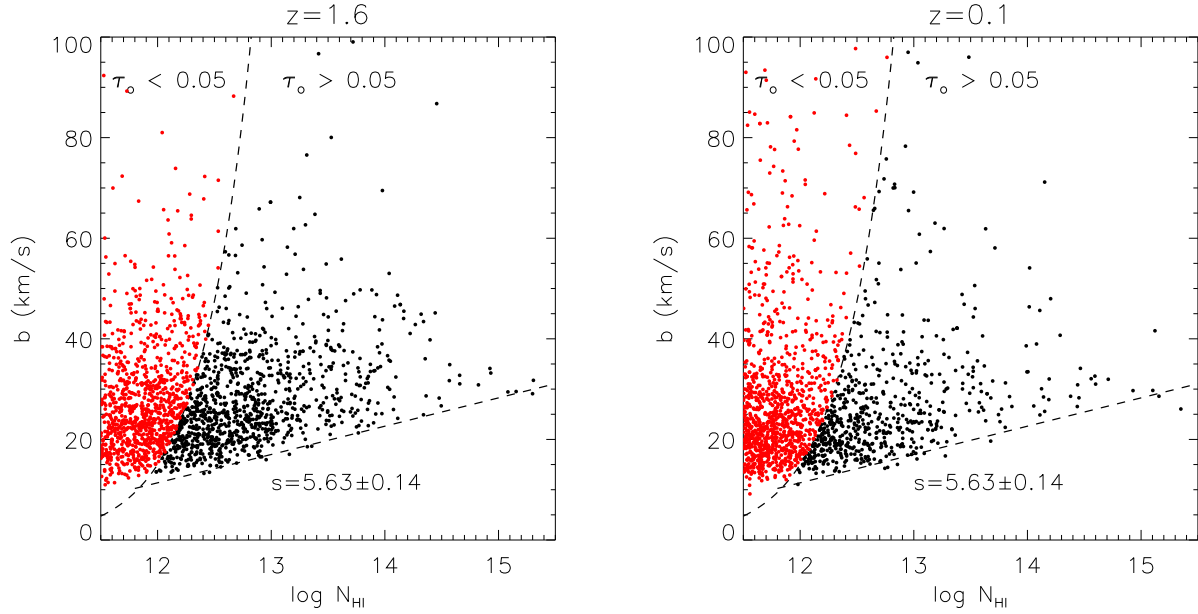


Figure 9. Each point shows the b -value and $\log N_{\text{HI}}$ value (cm^{-2}) of a Ly α line in one of the spectra at $z = 1.6$ (left) and $z = 0.1$ (right). We use 2000 randomly sampled spectra at $z=1.6$ and 1749 spectra at $z=0.1$. The relative number of points between the two redshifts corresponds to the ratio between the logarithm of the number of lines at $z=1.6$ (85817) and $z=0.1$ (20637) in the column density range of the plot, $\log N_{\text{HI}} = 11.5 - 15.5 \text{ cm}^{-2}$. The dashed curve shows lines with central optical depth $\tau_o = 0.05$ from equation (4). Lines to the left of this curve have $\tau_o < 0.05$ and will be extremely hard to detect with HST spectra. The dashed straight lines is a linear fit to the minimum b -values, $b_{\text{min}} = (5.63 \pm 0.14) \log(N_{\text{HI}}/10^{13}) + (16.99 \pm 1.78) \text{ km s}^{-1}$. This is a fit to the minimum in each of 10 bins of width 0.2 from $\log N_{\text{HI}} = 12.5 - 14.5 \text{ cm}^{-2}$ at $z=1.6$. We show the same straight line at $z=0.1$.

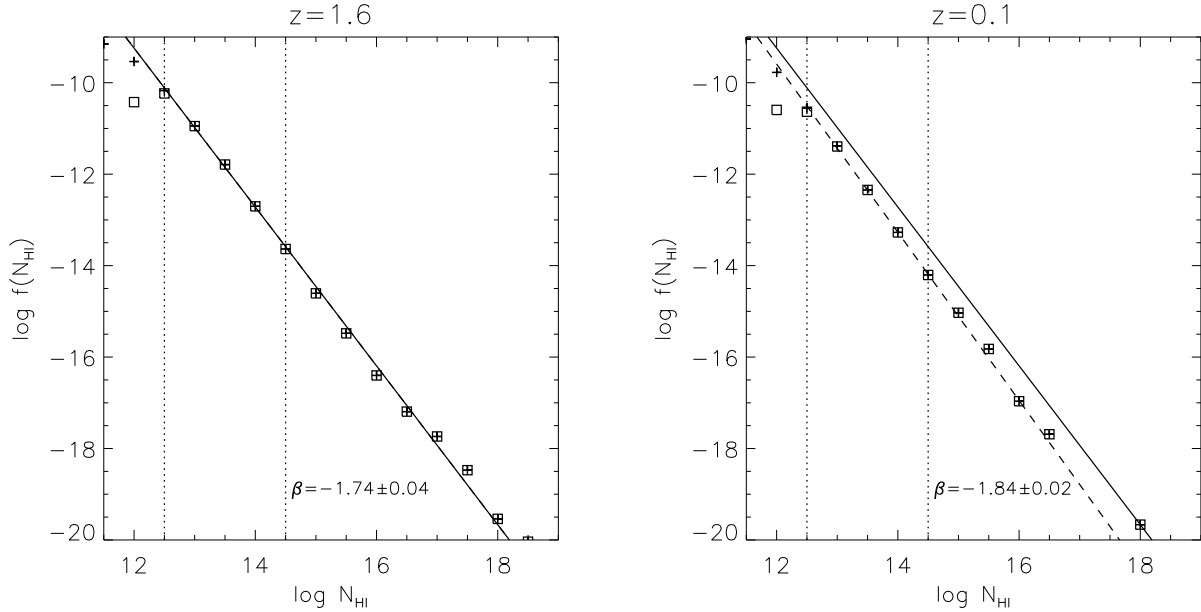


Figure 10. The column density distribution $f(N)$ at $z = 1.6$ and $z = 0.1$. The plus symbols show all lines with $\tau_o > 10^{-5}$, while the open squares are lines with $\tau_o > 0.05$. We show the same solid line on both plots. It is the power law, $f(N_{\text{HI}}) \propto N_{\text{HI}}^{\beta}$ that best fits the number of lines with $\tau_o > 10^{-5}$ and $\log N_{\text{HI}} = 12.5 - 14.5 \text{ cm}^{-2}$ in bins of 0.1, all at $z = 1.6$. The fit is $\log f(N_{\text{HI}}) = (-1.74 \pm 0.04) \log(N_{\text{HI}}/10^{12}) - (9.28 \pm 0.52)$. We extend the line to all $\log N_{\text{HI}}$ values. The dashed line is the power law fit at $z = 0.1$, $\log f(N_{\text{HI}}) = (-1.84 \pm 0.02) \log(N_{\text{HI}}/10^{12}) - (9.61 \pm 0.34)$, for the same column density range.

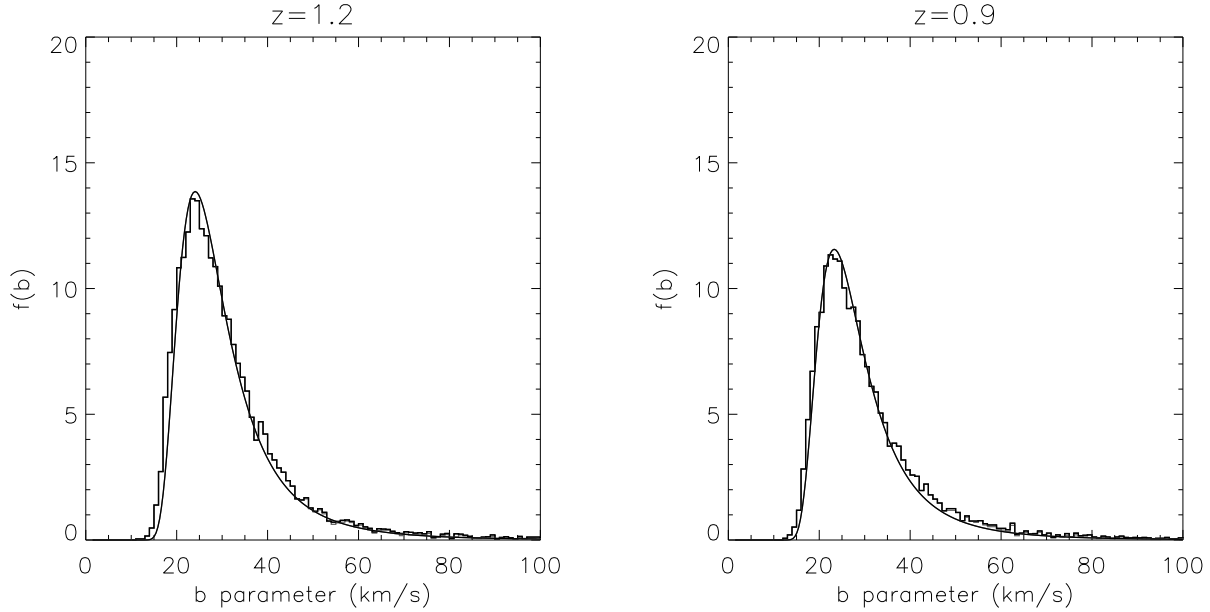


Figure 11. The distribution of the b -values $f(b) = d^2n/dzdb$ of $\text{Ly}\alpha$ lines with $\log N_{\text{HI}} = 12.5 - 14.5 \text{ cm}^{-2}$. The histogram shows the values in 1 km s^{-1} wide bins while the curve shows the Hui-Rutledge function. The area under the histograms and curves is the number lines per unit redshift with $12.5 < \log N_{\text{HI}} < 14.5 \text{ cm}^{-2}$.

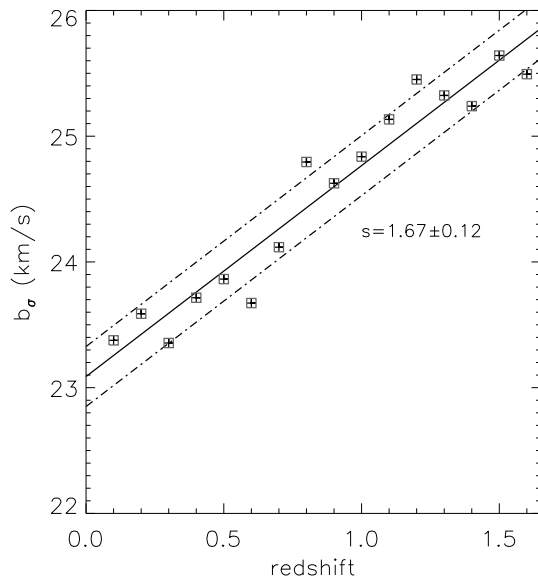


Figure 12. The redshift evolution of b_σ from Table 5 from the simulated spectra. The solid line is a linear fit in the form $b_\sigma = (1.67 \pm 0.12) * z + (23.09 \pm 0.11) \text{ km s}^{-1}$. The curves above and below the solid line are best fits to the 2σ upper and lower limits on the individual points. They do not show the range of possible fits.

W_o^t depends on redshift. We see that power laws are fair representations for all z and W_o^t values.

In Fig. 17 we show the equivalent widths as a function of column density. For low column densities, lines are unsaturated and on the linear portion of the curve of growth,

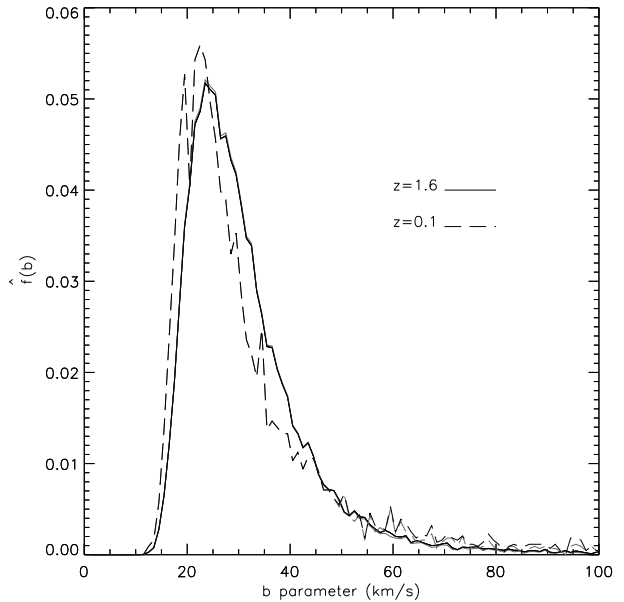


Figure 13. The doppler parameter distribution at two different redshifts. The distribution functions both have unit area.

where $W_o \propto \log N_{\text{HI}}$, there is no dependence on the b -value. These are the most common lines with $\log N_{\text{HI}} \sim 14 \text{ cm}^{-2}$ and $W_o \sim 0.3 \text{ \AA}$. However, for larger $\log N_{\text{HI}}$ values, the lines become saturated and the W_o depends on the b -value. We see that when $W_o > 0.5 \text{ \AA}$ we have some lines with very large column densities. The simulation has factors of several too few lines with $\log N_{\text{HI}} > 17 \text{ cm}^{-2}$ at $z = 2$, and hence it also lack lines with $W_o > 0.5 \text{ \AA}$. For saturated lines with a fixed $\log N_{\text{HI}}$ value, we obtain a larger

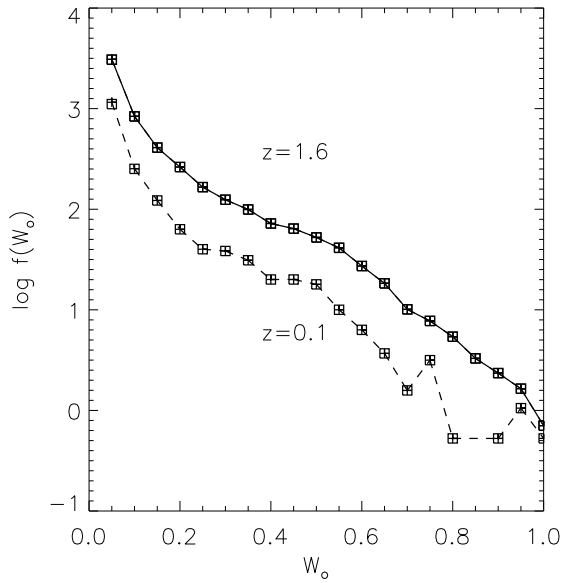


Figure 14. The equivalent width distribution, defined as $f(W_o) = d^2n/dz dW_o$, shown at $z = 1.6$ and $z = 0.1$. W_o is the rest frame equivalent width of an absorption line in units of \AA . The distribution is computed in bins of size 0.05 in equivalent width and is shown for $W_o \geq 0.025$, the left edge of the first bin which is centered at $W_o = 0.05$. The solid and dashed lines refer to $z = 1.6$ and $z = 0.1$ respectively. Compared to data at $z = 2$, our simulation lacks Ly α lines with $\log N_{\text{HI}} > 17 \text{ cm}^{-2}$ or $W_o > 0.5 \text{ \AA}$.

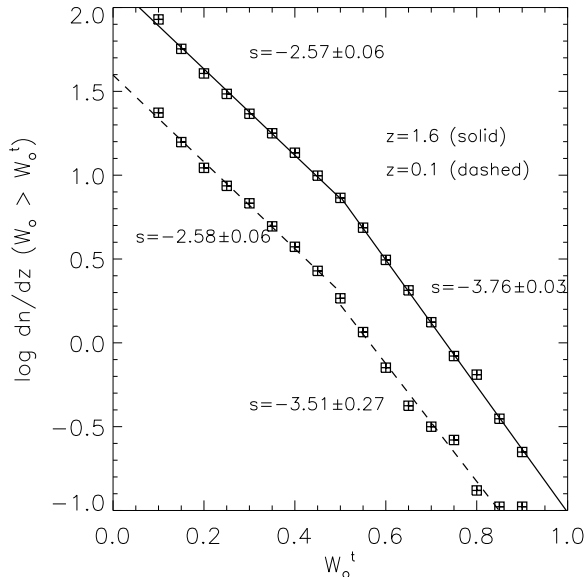


Figure 15. The number of lines per unit z with equivalent width exceeding W_o^t (\AA ngstroms). We show the results for $z = 1.6$ (above) and $z = 0.1$ (below). The straight lines with slopes s join at $W_o^t = 0.5$. Compared to data at $z = 2$ our simulation lacks Ly α lines with $W_o > 0.5 \text{ \AA}$.

Table 5. Line widths as a function of redshift in simulated spectra. We list the Hui-Rutledge b_σ parameter and the median b -value b_{med} from lines with $\tau_o > 0.05$. The last column contains the log of the number of lines per unit z with $\log N_{\text{HI}} = 12.5$ – 14.5 cm^{-2} .

z	b_σ	b_{med}	$\log(dn/dz)$
1.6	25.49	28.38	2.53
1.5	25.64	28.25	2.50
1.4	25.24	28.16	2.46
1.3	25.32	28.13	2.43
1.2	25.45	28.03	2.40
1.1	25.13	27.97	2.37
1.0	24.84	27.82	2.34
0.9	24.62	27.36	2.31
0.8	24.79	27.33	2.29
0.7	24.12	27.08	2.25
0.6	23.67	27.04	2.23
0.5	23.86	26.90	2.21
0.4	23.71	26.75	2.19
0.3	23.35	26.72	2.15
0.2	23.59	26.65	2.11
0.1	23.38	26.62	2.08

Table 6. The equivalent width distribution, $f(W_o)$, with W_o in \AA , at different redshifts. A value of N/A means there were no lines at that equivalent width for that redshift.

W_o	redshift					
	1.6	1.3	1.0	0.7	0.4	0.1
0.05	3.490	3.380	3.299	3.199	3.160	3.064
0.10	2.923	2.826	2.738	2.655	2.583	2.403
0.15	2.613	2.513	2.428	2.330	2.208	2.087
0.20	2.419	2.289	2.225	2.112	1.976	1.801
0.25	2.220	2.137	1.997	1.882	1.787	1.602
0.30	2.094	2.003	1.926	1.727	1.531	1.585
0.35	1.997	1.873	1.662	1.625	1.501	1.492
0.40	1.858	1.804	1.643	1.523	1.328	1.301
0.45	1.807	1.696	1.582	1.464	1.372	1.301
0.50	1.719	1.591	1.464	1.376	1.420	1.253
0.55	1.616	1.542	1.302	1.256	1.201	1.000
0.60	1.435	1.325	1.258	0.981	0.957	0.801
0.65	1.263	1.154	1.041	0.926	0.860	0.567
0.70	1.004	0.957	0.852	0.584	0.355	0.199
0.75	0.889	0.717	0.740	0.583	0.355	0.500
0.80	0.733	0.341	0.464	0.487	0.258	-0.278
0.85	0.517	0.216	N/A	0.062	-0.042	N/A
0.90	0.371	0.392	-0.189	-0.115	-0.343	-0.278
0.95	0.216	0.040	-0.013	-0.416	-0.343	0.023
1.00	-0.151	0.040	N/A	N/A	N/A	-0.278

W_o value when the b -value is larger which allows more of the atoms to absorb photons because they are more widely distributed in velocity. Hence the lines with $W_o \sim 1 \text{ \AA}$ and $\log N_{\text{HI}} \sim 14.5 \text{ cm}^{-2}$ have large b -values while those with $W_o \sim 0.5 \text{ \AA}$ and $\log N_{\text{HI}} > 16 \text{ cm}^{-2}$ have small b -values. We know from Misawa et al. (2004, Figs. 3 & 5) that at $z = 2.5$ some such lines have b -values smaller than those of any lines with $\log N_{\text{HI}} \sim 14 \text{ cm}^{-2}$. Note that the total W_o from all lines in the simulated spectra with $\log N_{\text{HI}} > 17 \text{ cm}^{-2}$ is negligible and hence these lines have a negligible effect on most statistics. We do not know how many lines we might see in a simulation with much smaller cell size and self-shielding.

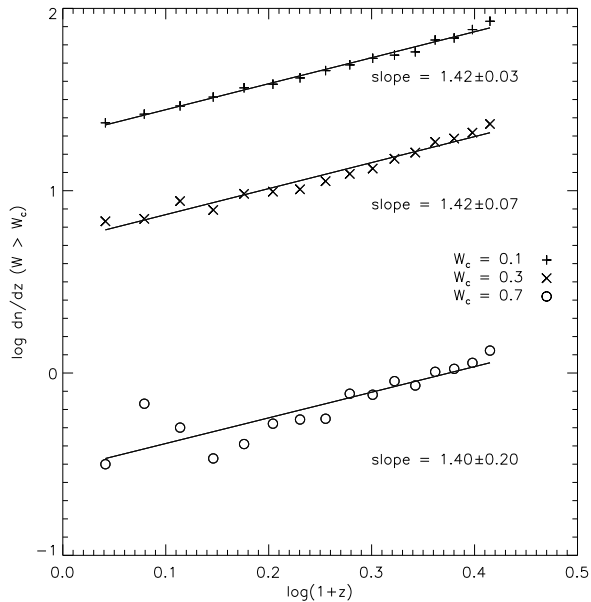


Figure 16. The redshift evolution of the number of lines exceeding equivalent width $W_o=0.1, 0.3$ or 0.7 Ångstroms. We also show power laws $dn/dz \propto (1+z)^\gamma$ with slopes γ .

4.5 Number of Lines per unit redshift

We show the number of lines per unit redshift in Fig. 18 for both the large sample of lines with $\tau_o > 10^{-5}$ and the sub-sample with $\tau_o > 0.05$. Note the dramatic difference! The large sample shows a factor of a few more lines at lower redshifts, while the sub-sample, that is a better representation of data, shows the opposite. The number of lines is clearly very sensitive to the definition of the sample (Zhang et al. 1997), yet in both cases the change with redshift is very well described by a single power law.

In Fig. 19 we examine the redshift evolution of the number of lines with very high column densities, $\log N_{\text{HI}} > 16$ and $\log N_{\text{HI}} > 17 \text{ cm}^{-2}$. The lines with $\log N_{\text{HI}} > 17 \text{ cm}^{-2}$ evolve more quickly. We should remind the reader that our simulation has factors of many too few lines with these column densities because it is optically thin and the cell size is factors of many too large.

We show in Fig. 20 the number of Ly α lines above a cutoff column density at redshifts of 1.6 and 0.1. We see an excess of lines above the power law fit at $z = 1.6$ for $\log N_{\text{HI}} > 16 \text{ cm}^{-2}$. This excess is less at lower redshifts and it almost disappears by $z = 0.1$.

5 COMPARISON TO DATA

Our simulations have known limitations. They lack high column density lines compared to simulations that have much smaller cell size and allow self-shielding. We also know that at $z = 2$ there are differences between simulated and real spectra that show up in most statistics (Tytler et al. 2007).

When we compare to data we would ideally match the properties of the observed spectra in detail, including the z range, signal-to-noise ratio, spectral resolution and continuum errors. In this section, we compare statistics of the Ly α

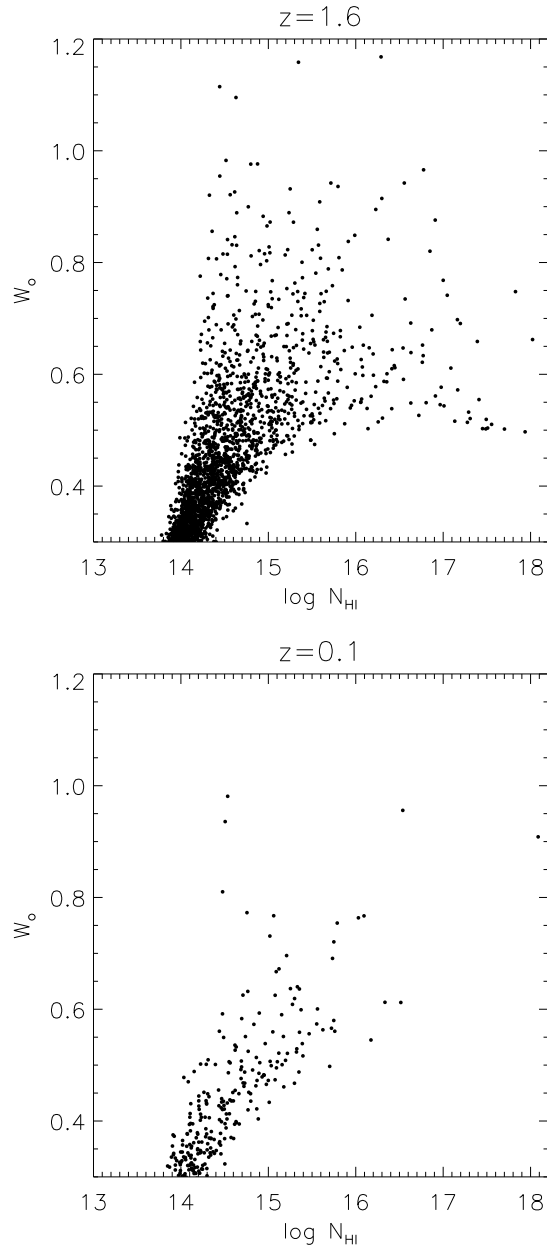


Figure 17. The equivalent widths (Ångstroms) and H I column densities (cm^{-2}) of Ly α lines at $z = 1.6$ and $z = 0.1$. We show all lines in the plot range from all 2000 simulated spectra at each redshift, except for four with $\log N_{\text{HI}} > 18.2 \text{ cm}^{-2}$ at $z = 1.6$.

forest in real and simulated spectra. We will ignore spectral resolution and the signal-to-noise ratio of the real spectra, although we will attempt to match the redshift and column density ranges.

Kirkman et al. (2007) measure the mean amount of absorption in the Ly α forest at low redshifts using *HST* spectra of 74 QSOs. In Fig. 21 we show that our DA values are very close to the observed ones from Kirkman et al. (2007, Table 5), where we do not consider the dip in DA at $z = 1.4$ to be significant.

Janknecht et al. (2006) fit the column densities and b -values to lines in HST spectra of 9 QSOs at $z_{\text{em}} < 1.94$.

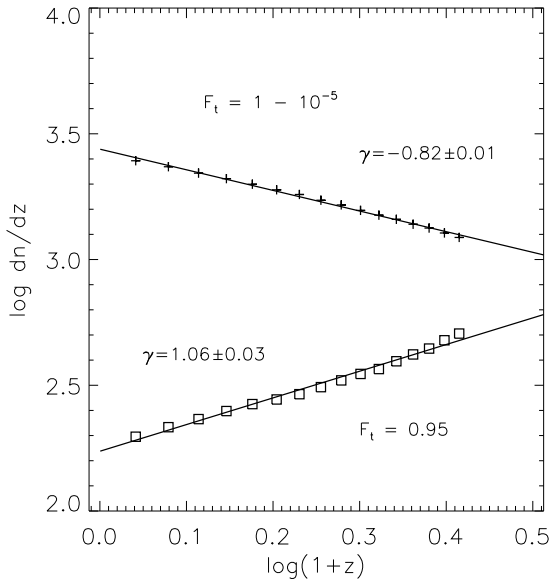


Figure 18. The number of lines with central optical depth $\tau_o > 10^{-5}$ (plus symbols) or $\tau_o > 0.05$ (open squares). We also show power laws $dn/dz = A(1+z)^\gamma$, with $A = 3.439 \pm 0.004$ and $\gamma = -0.820 \pm 0.014$ for $\tau_o > 10^{-5}$ (above) and $A = 2.24 \pm 0.01$ and $\gamma = 1.06 \pm 0.03$ for $\tau_o > 0.05$ (below).

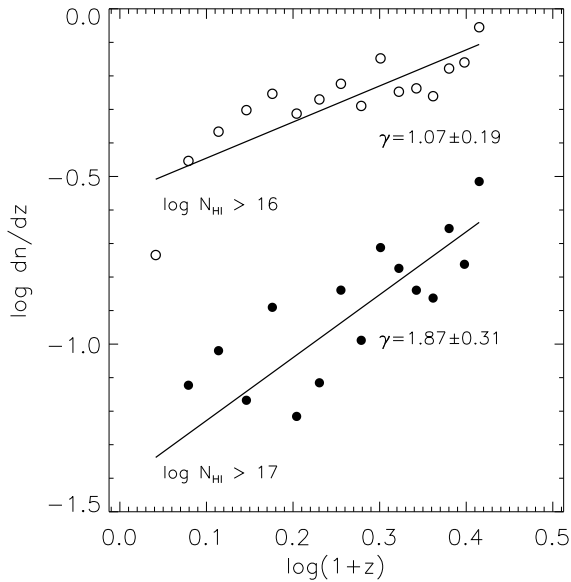


Figure 19. The redshift evolution of number of lines with $\log N_{\text{HI}} > 16 \text{ cm}^{-2}$ (open circles) and $\log N_{\text{HI}} > 17 \text{ cm}^{-2}$ (filled circles). The straight lines are power laws $dn/dz \propto (1+z)^\gamma$.

They fit the column density distribution with a power law $f(N) = A \log N_{\text{HI}}^\beta$ and find no significant change of the power with redshift, just as we do. They find a power law of $\beta \simeq 1.57 \pm 0.05$ consistent with our value of ~ 1.62 .

The median b -values from the HST spectra, 28 km s^{-1} , and from our simulation, 28.5 km s^{-1} , are also very similar,

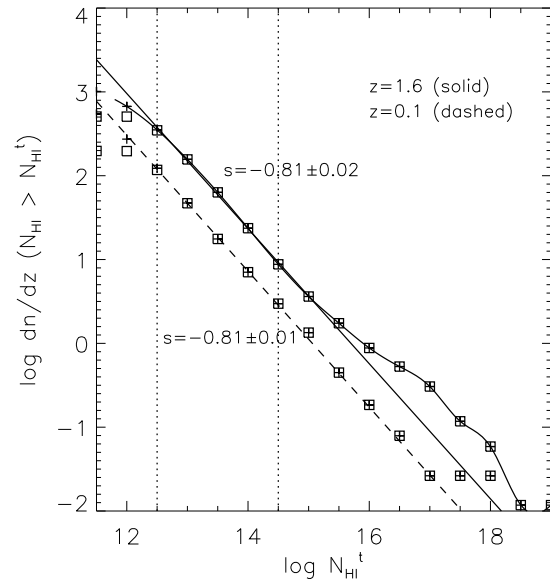


Figure 20. The number of lines per unit redshift as a function of the minimum column density at $z = 1.6$ and $z = 0.1$. We show both the large sample of lines (plus symbols) and the subsample with $\tau_o > 0.05$ (open squares). The solid straight line is a power law fit at $z = 1.6$ (plus symbols) to $\log N_{\text{HI}}^t = 12.5 - 14.5 \text{ cm}^{-2}$ (vertical dotted lines). The dashed straight line is the corresponding fit to the $z = 0.1$ points.

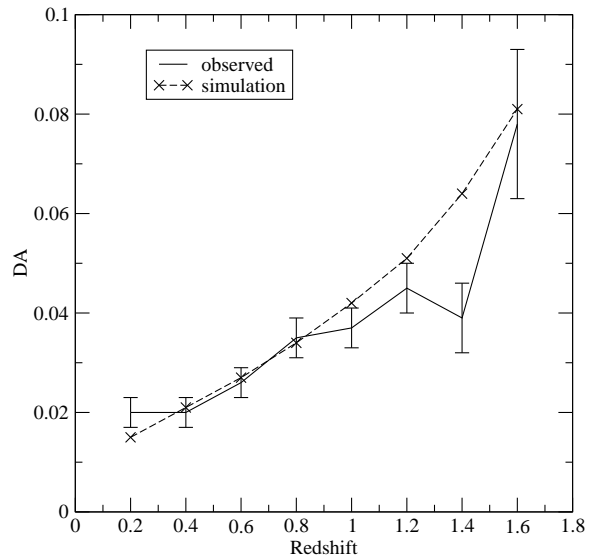


Figure 21. Comparison of the mean amount of absorption, DA values, in HST spectra (error bars) from Kirkman et al. (2007), and in the simulated spectra (crosses). We have not adjusted the the simulation output or spectra in any way.

Table 7. Comparison of Ly α lines in HST spectra (Janknecht et al. 2006) and in our simulated spectra. The HST spectra have 270 lines at $z = 0.5 - 1.0$ and 595 lines at $z = 1.0 - 1.5$. β is the index on the power law equation of the distribution of column densities, $f(N)$. The median line width is b_{med} (km s $^{-1}$) and b_σ is the Hui-Rutledge parameter.

z	β obs	β sim	b_{med} obs	b_{med} sim	b_σ obs	b_σ sim
0.5 - 1.0	1.57 ± 0.05	1.62	29	28.3	18.9	25
1.0 - 1.5	1.58 ± 0.04	1.63	28	28.5	23.5	25.5

see Table 7. However, our b_σ values are larger than those in the HST spectra. We have two comments on the b_σ values. It is well known that samples of lines from spectra with significant noise, including all HST spectra, include an excess of lines with low b -values. Common lines with the lowest column densities enter the sample when photon noise gives them extra depth in one or two pixels; see Kirkman & Tytler (1997, Fig. 10 & 11) or Misawa et al. (2004, Fig. 3). We saw in J05 that the simulation also makes lines that are too wide at $z = 2$ and that smaller cells would reduce the line widths but not enough to resolve the difference. We discussed this issue at length in Tytler et al. (2007).

6 CONCLUSIONS

Some statistical descriptions of the Ly α forest vary greatly over the redshift range $z = 0.1 - 1.6$ while others change little. Statistics that change greatly derive from the mean amount of absorption: the flux pdf, the power and auto correlation of the flux, and the amplitude of $f(N)$ and the number of lines per unit z . The statistics that change little relate to the line widths: the shape (not the amplitude) of the b -value distribution, $f(b)$, the b_σ value and the b - N distribution.

The changes in the Ly α forest with redshift are all exceedingly smooth, with a constant rate of change across the redshift range 0.1 - 1.6. There are no special redshifts and no need for “broken” power laws or changes in slope. We can readily predict the values of parameters at larger or smaller redshifts. Specifically, we do not see the jump in the evolution of the number of lines number of lines per unit z , as reported by Weymann et al. (1998). Rather, our results are very close to the constant rate of evolution found in recent analysis of larger samples of HST spectra by Janknecht et al. (2006) and Kirkman et al. (2007).

We have found good agreement between the main statistics of the Ly α forest lines in HST spectra and in our simulated spectra. These statistics include the mean amount of absorption, the change in the absorption with redshift and the median b -value. The b_σ is smaller in HST spectra than in our simulations. This difference might be real, but given the agreement in the median b -value, it is more likely a result of the low SNR of the HST spectra giving a false excess of narrow lines.

The agreement between the Ly α forest in our simulations and in HST spectra is better than we had anticipated. We already know that there are differences between the simulation and data at $z = 2$ but these are mostly too subtle to be detected in the existing HST spectra. The HST spectra

with high enough resolution to resolve Ly α lines are few and they have very low SNR by ground based standards. While we had adjusted the astrophysical parameters of the simulation to approximately match data at $z = 2$ we made no such adjustments for any lower redshifts. The evolution of the Ly α forest in the simulation is controlled by the change in the gas density, the growth of structure and especially the change in the ionisation and heating by the UVB. We know that the UVB intensity was adjusted by Haardt and Madau to match a variety of data at various redshifts, but they did not explicitly match the low redshift IGM using a simulation of the Ly α forest. They clearly did an excellent job of calculating the UVB at low redshifts. In this limited sense, our simulation is predicting the Ly α forest at low redshifts, and it is doing much better than we had expected. This implies that the simulation comes close to representing the main physical process in the IGM, those responsible for the appearance and evolution of the Ly α forest.

ACKNOWLEDGMENTS

This work was supported by NASA grant STScI AR-10688 and by NSF grant AST 0507717. We ran the simulation using the facilities of the NCSA SDSC supercomputer centres with LRAC allocation MCA98N020.

REFERENCES

- Abel T., Anninos P., Zhang Y., Norman M. L., 1997, *New Astronomy*, 2, 181
- Anninos P., Zhang Y., Abel T., Norman M. L., 1997, *New Astronomy*, 2, 209
- Barkana R., Loeb A., 2004, *ApJ*, 609, 474
- Bodenheimer P., Laughlin G. P., Rózyczka M., Yorke H. W., eds, 2007, *Numerical Methods in Astrophysics: An Introduction*
- Bolton J., Meiksin A., White M., 2004, *MNRAS*, 348, L43
- Bolton J. S., Viel M., Kim T. ., Haehnelt M. G., Carswell R. F., 2007, *ArXiv e-prints*, 711
- Bryan G. L., Norman M. L., 1997, in Clarke D. A., West M. J., eds, *Computational Astrophysics; 12th Kingston Meeting on Theoretical Astrophysics Vol. 123 of Astronomical Society of the Pacific Conference Series, Simulating X-Ray Clusters with Adaptive Mesh Refinement*. p. 363
- Bryan G. L., Norman M. L., Stone J. M., Cen R., Ostriker J. P., 1995, *Computer Physics Communications*, 89, 149
- Davé R., Hernquist L., Katz N., Weinberg D. H., 1999, *ApJ*, 511, 521
- Eisenstein D. J., Hu W., 1999, *ApJ*, 511, 5
- Haardt F., Madau P., 2001, in *Clusters of galaxies and the high redshift universe observed in X-rays, Recent results of XMM-Newton and Chandra, XXXVIth Rencontres de Moriond, XXIst Moriond Astrophysics Meeting, March 10-17, 2001, Savoie France*. Edited by D.M. Neumann & J.T.T. Van Modelling the UV/X-ray cosmic background with CUBA
- Hui L., Rutledge R. E., 1999, *ApJ*, 517, 541
- Janknecht E., Reimers D., Lopez S., Tytler D., 2006, *â*, 458, 427

- Jena T., Norman M. L., Tytler D., Kirkman D., Suzuki N., Chapman A., Melis C., Paschos P., O'Shea B., So G., Lubin D., Lin W., Reimers D., Janknecht E., Fechner C., 2005, MNRAS, 361, 70
- Kim T.-S., Bolton J. S., Viel M., Haehnelt M. G., Carswell R. F., 2007, MNRAS, 382, 1657
- Kirkman D., Tytler D., 1997, ApJ, 484, 672
- Kirkman D., Tytler D., Lubin D., Charlton J., 2007, MNRAS, 376, 1227
- Kohler K., Gnedin N. Y., 2007, ApJ, 655, 685
- Meiksin A., White M., 2004, MNRAS, 350, 1107
- Misawa T., Tytler D., Iye M. Paschos P., Norman M., Kirkman D., O'Meara J., Suzuki N., Kashikawa N., 2004, AJ, [astroph/0303476](#), 128, 2954
- Norman M. L., Bryan G. L., 1999, in ASSL Vol. 240: Numerical Astrophysics Cosmological Adaptive Mesh Refinement. p. 19
- Norman M. L., Bryan G. L., Harkness R., Bordner J., Reynolds D., O'Shea B., Wagner R., 2007, ArXiv e-prints, 705
- O'Shea B. W., Bryan G., Bordner J., Norman M. L., Abel T., Harkness R., Kritsuk A., 2004, in Adaptive Mesh Refinement – Theory and Applications. Eds. T. Plewa, T. Linde & V.G. Weirs, Springer Lecture Notes in Computational Science and Engineering. Introducing ENZO, an AMR cosmology application
- O'Shea B. W., Nagamine K., Springel V., Hernquist L., Norman M. L., 2005, ApJS, 160, 1
- Paschos P., Norman M. L., Bordner J. O., Harkness R., 2007, ArXiv e-prints
- Pen U.-L., 1997, ApJ, 490, L127
- Regan J. A., Haehnelt M. G., Viel M., 2007, MNRAS, 374, 196
- Sirko E., 2007, PhD thesis, Princeton University
- Spitzer L., 1978, Physical Processes in the Interstellar Medium. New York:Wiley
- Tytler D., 1987, ApJ, 321, 49
- Tytler D., Kirkman D., O'Meara J., Suzuki N., Orin A., Lubin D., Paschos P., Jena T., Lin W.-C., Norman M., 2004, ApJ, 617, 1
- Tytler D., Paschos P., Kirkman D., Norman M., Jena T., 2007, ArXiv e-prints
- Weymann R. J., Jannuzi B. T., Lu L., Bahcall J. N., Bergeron J., Boksenberg A., Hartig G. F., Kirhakos S., Sargent W. L. W., Savage B. D., Schneider D. P., Turnshek D. A., Wolfe A. M., 1998, ApJ, 506, 1
- Zhang Y., Anninos P., Norman M. L., Meiksin A., 1997, ApJ, 485, 496